Tailoring the performance of ZnO for oxygen evolution by effective transition metal doping

Qiuhua Liang,[a,c] Geert Brocks,*[b,c,d] Vivek Sinha,[a,e] and Anja Bieberle-Hütter*[a, b]

[a]   Q. Liang, Dr. V. Sinha, Dr. A. Bieberle-Hütter
        Electrochemical Materials and Interfaces (EMI), Dutch Institute for Fundamental Energy Research (DIFFER), De Zaale 20, 5612 AJ, Eindhoven, the Netherlands.
        E-mail: a.bieberle@differ.nl
[b]   Prof. G. Brocks, Dr. A. Bieberle-Hütter
        Center for Computational Energy Research (CCER), P.O. Box 513, 5600 MB, Eindhoven, the Netherlands.
        E-mail: g.h.l.a.brocks@utwente.nl
[c]   Q. Liang, Prof. G. Brocks
        Materials Simulation and Modeling (MSM), Department of Applied Physics, Eindhoven University of Technology, P.O. Box 513, 5600MB, Eindhoven, the Netherlands.
[d]   Prof. G. Brocks
        Computational Materials Science, Faculty of Science and Technology and MESA+ Institute for Nanotechnology, University of Twente, P.O. Box 217, 7500 AE Enschede, the Netherlands.
[e]   Dr. V. Sinha
        Process and Energy (P&E) Department, Faculty of Mechanical, Maritime and Materials Engineering (3mE), Delft University of Technology, Leeghwaterstraat 39, 2628CB, Delft, The Netherlands.

        Supporting information for this article is given via a link at the end of the document.

Abstract: In the quest for active and inexpensive (photo)electrocatalysts, atomistic simulations of the oxygen evolution reaction (OER) are essential for understanding the catalytic process of water splitting at solid surfaces. In this paper, we study the enhancement of the OER by first-row transition-metal (TM) doping of the abundant semiconductor ZnO, using density functional theory (DFT) calculations on a substantial number of possible structures and bonding geometries. The calculated overpotential for undoped ZnO is 1.0 V. For TM dopants in the 3d series from Mn to Ni, the overpotentials decrease from 0.9 V for Mn, and 0.6 V for Fe, down to 0.4 V for Co, and rise again to 0.5 V for Ni and 0.8 eV for Cu. We analyze the overpotentials in terms of the binding to the surface of the species involved in the four reaction steps of the OER. The Gibbs free energies associated with the adsorption of these intermediate species increase down the series from Mn to Zn, but the difference between OH and OOH adsorption (the species involved in the first, respectively the third reaction step) is always in the range 3.0-3.3 eV, despite a considerable variation in possible bonding geometries. The bonding of the O intermediate species (involved in the second reaction step), which is optimal for Co, and to a somewhat lesser extend for Ni, then ultimately determines the overpotential. These results imply that both Co and Ni are promising dopants for increasing the activity of ZnO-based anodes for the OER.

Introduction

Water splitting is a promising technology for future generation and storage of clean and sustainable energy. Electrolytic water splitting comprises two reactions, the oxygen evolution reaction (OER) at the anode and the hydrogen evolution reaction (HER) at the cathode.[1] Current research strongly focuses on OER, as it is the bottleneck in terms of poor energy efficiency and slow reaction rate. The OER is a four-electron process that is more complicated than the two-electron process of the HER.[2] Current understanding models these as multi-step reactions with a single electron transfer at each step. Each of these steps is potentially unfavorable thermodynamically or kinetically, which to overcome then requires an overpotential in the electrolytic cell.[3] Platinum-group metal containing catalysts, such as RuO_2 and IrO_2, are considered state-of-the-art OER catalysts owing to their relatively small overpotentials,[4] but their high costs and scarcity severely hinder large scale applications. Therefore, it is crucial to explore alternative OER catalysts with high catalytic activity, good stability, abundance, and low costs, where the most obvious direction is towards catalysts based on earth-abundant 3d metals.

Recently, precious-metal-free catalysts based on earth-abundant 3d metals, such as transition metal (TM) nitrides,[5] phosphides,[6] oxides,[3, 7] sulfides,[8] and MXenes[9] have gained attention. In particular, TM oxides have been considered as potential substitutes for Pt-based catalysts due to their low cost and excellent chemical stability.[10] Photoelectrolytic water splitting in integrated devices poses extra demands on electrode materials, the most obvious ones being that they should not block photon absorption, have a decent conductivity, and be stable in contact with an (alkaline or acidic) electrolyte, which all point in the direction of doped, transparent oxide semiconductors. In this respect, ZnO is expected to be a good candidate due to its large band gap, good (semi)conducting properties,[11] low cost, non-toxicity, appropriate redox potential, and high electrochemical stability.[12] However, pure ZnO shows a rather poor OER activity,[13],[14] and to make it suitable, one should enhance its OER performance, for instance by doping or by nano-structuring.[15] Jang et al.[14] have experimentally studied composites of ZnO and 3d TM (Mn, Fe, Co, Ni) oxides and found that all these composites exhibit a greatly enhanced OER activity, as compared to pure ZnO.

Composites are, however, a rather drastic way of combining TMs with ZnO, which can have a large impact on its (micro)structure, and its optical and electronic properties. We suggest a milder route, which involves incorporating 3d TM atoms in the ZnO lattice as substitutional dopants. This type of doping has been identified as an effective way to enhance the OER activity.[14, 16] The dopant atom serves both as a trapping site for a charge carrier, thereby localizing it, as well as a catalytic reaction center for the OER. In the present paper, we study 3d TM doped ZnO with respect to OER activity by means of first-principles

density-functional-theory (DFT) calculations, exploring a large range of possible structures of dopants and absorbed species involved in the OER.

Results and Discussion

GGA+U functional

It is well-known that the PBE functional severely underestimates the band gap of ZnO, where our findings agree with previously obtained results,[17] see Figure S1 in the Supporting Information. Previous DFT studies have used the PBE+U method to correct for this band gap error.[18] Note however that an accurate description of the band gap can be obtained only by using parameters that are physically not extremely well justified, such as U_O on the oxygen 2p states besides U_{Zn} on the zinc 3d states.[19] We have tested the PBE+U functional, treating the on-site electron-electron Coulomb and exchange interactions within the Dudarev et al. approach,[20] for a range of values for U_{Zn} and U_O, as suggested by the literature.[18] More details are discussed in Sec 1 of the Supporting Information. We find, in agreement with the literature, that inclusion of U, can indeed markedly improve the band gap, see Figures S2 and S3. However, whereas the optimized lattice parameters calculated with the standard PBE functional (a = 3.28 Å, c = 5.30 Å) are in reasonable agreement with the experimental values (a = 3.25 Å, c = 5.21 Å),[21] those calculated with the PBE+U functionals are significantly too small, the largest deviation being presented by the cases with the best band gap, for more details see Sec 1.1 in Supporting Information. Straining the lattice leads to changes in the OER performance,[22] which renders the applicability of the PBE+U functional for calculations on the OER questionable.

Using a hybrid functional, such as PBE0, would a better way to obtain a better band gap without deteriorating the structure of ZnO.[23] However, calculations with hybrid functionals increase the computational costs by one to two orders of magnitude.[19] In our case we need to perform a large number of geometry optimizations on sizable supercells and slabs, the costs of which prohibit the use of a hybrid functional. Therefore, we hold on to the PBE functional (and PBE optimized structures).

Upon substitution of Zn atoms in ZnO by first-row TM atoms, the 3d states of the latter contribute to the valence band, but can also appear as defect states in the ZnO band gap, see Figure S4. Therefore, it is possible that the electronic structure of TM substituent atoms is affected by a ZnO band gap that is too small. The 3d states decrease in energy along the TM series from Sc to Cu. With the PBE functional we find that the 3d states in the series from Sc to Cr overlap with the ZnO conduction band, and partially lose their electrons, see Table S1. We test whether the PBE+U functional improves this description. The magnetic moments of the TM-doped ZnO slab calculated with the PBE+U functional, as shown in Table S2 for the TM dopants Sc to Cr. Comparison to the results shown in Table S1 demonstrates that enlarging the band gap of ZnO using the PBE+U functional actually changes the magnetic moments very little. Qualitatively this does not change even if PBE-optimized structures are used. Whereas these cases may require further study, these particular TM atoms are in fact of small interest. Their catalytic activity is expected to be small, exactly because of the high energy of the 3d states, which results in a strong bonding to oxygen species, and a high overpotential.[16a] Therefore, we will not discuss the early TMs from Sc to Cr further.

The 3d states of substitutions by late TM atoms, Mn to Cu, show no overlap with the ZnO conduction band, see Figure S4, and are thus not affected by a band gap that is too small. Moreover, these late TM substitutions may be expected to have significant catalytic activity.[16a] Our calculations therefore focus on the series from Mn to Cu.

It should be noted that all TM dopant atoms are found in high-spin states corresponding to a valency of 2+, and a configuration $4s^0 3d^n$, n = 5-10 for Mn-Zn, as demonstrated by their calculated magnetic moment and the projected density of states (PDOS), see the Table S6 and Figure S4.

OER Mechanism and Free Energies

We assume liquid water under alkaline conditions as the electrolyte, which gives the following overall OER at the anode[24]

$$4OH^- \rightarrow O_2 + 2H_2O + 4e^-. \tag{1}$$

This four-electron OER is broken down into four elementary reaction steps, which is believed to be the dominant reaction mechanism for TM oxides under alkaline conditions.[14, 24b, 25]

$$* + OH^- \rightarrow {}^*OH + e^-, \tag{2}$$
$$^*OH + OH^- \rightarrow {}^*O + H_2O(l) + e^-, \tag{3}$$
$$^*O + OH^- \rightarrow {}^*OOH + e^-, \tag{4}$$
$$^*OOH + OH^- \rightarrow * + O_2(g) + H_2O(l) + e^-, \tag{5}$$
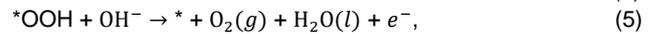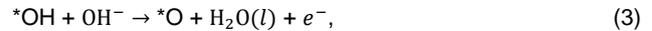
where * represents an adsorption site on the catalyst surface; *OH, *O, and *OOH are the intermediate reactant species adsorbed on the active site, and (g) and (l) indicate the gas phase and the liquid phase, respectively.

The Gibbs free energies and overpotentials that characterize the OER are calculated by the computational hydrogen electrode (CHE) approach developed by Rossmeisl et al.[26] To calculate the difference in Gibbs free energies $G_{OH^-} - G_{e^-}$, which is needed in describing reactions (2)-(5), we assume the equilibria $H_2O(l) \leftrightharpoons H^+ + OH^-$, and $H^+(aq) + e^- \leftrightharpoons \frac{1}{2}H_2(g)$ at standard conditions, P = 1 bar and T = 298 K.

We then have

$$G_{OH^-} - G_{e^-} = G_{H_2O(l)} - G_{H^+} - G_{e^-} = G_{H_2O(l)} - \frac{1}{2}G_{H_2} + eU, \tag{6}$$

where U is the potential with respect to the reversible hydrogen electrode (RHE).[27] Using (6), the Gibbs free energies of reactions (2)-(5) are then given by

$$\Delta G_1 = E_{^*OH} - E_* - E_{H_2O} + \frac{1}{2}E_{H_2} + (\Delta ZPE - T\Delta S)_1 - eU, \tag{7}$$
$$\Delta G_2 = E_{^*O} - E_{^*OH} + \frac{1}{2}E_{H_2} + (\Delta ZPE - T\Delta S)_2 - eU, \tag{8}$$
$$\Delta G_3 = E_{^*OOH} - E_{^*O} - E_{H_2O} + \frac{1}{2}E_{H_2} + (\Delta ZPE - T\Delta S)_3 - eU, \tag{9}$$
$$\Delta G_4 = \Delta G_0 - \Delta G_1 - \Delta G_2 - \Delta G_3 - 4eU. \tag{10}$$

where ΔG_0 = 4.92 eV is the Gibbs free energy of the overall reaction (1); E_{*X} are the DFT calculated total energies of the substrate with adsorbed species X, and E_Y are the DFT calculated total energies of molecule Y; ΔZPE and $T\Delta S$ are the changes in zero-point energies and entropy contributions related to the different adsorbed species, see the Computational Methods section. ZPE corrections and entropic contributions (TS) to the free energies are listed in Table S3. Note that in Eq (10) we make use of the sum rule

$$\Delta G_0 = \Delta G_1 + \Delta G_2 + \Delta G_3 + \Delta G_4, \tag{11}$$

to avoid having to calculate E_{O_2}, which is problematic in DFT because of the open shell character of the O_2 molecule.

For the ideal catalyst, all four reaction steps should involve equal Gibbs free energy changes

$$\Delta G_1 = \Delta G_2 = \Delta G_3 = \Delta G_4 = \Delta G_0/4 = 1.23 \text{ eV}, \tag{12}$$

at potential U = 0, implying that at $U \geq 1.23$ eV reactions (2)-(5) become thermodynamically favorable. In reality, the four steps will not have the same reaction Gibbs free energy, which then leads to an overpotential to initiate the reaction step with the largest free energy. The overpotential is thus defined as

$$\eta = (\max[\Delta G_n] - \Delta G_0/4)/e \quad \text{where } n = 1,2,3,4. \quad (13)$$

Doping Configurations and Adsorption Sites

The $(10\bar{1}0)$ surface of the ZnO wurtzite, which is the most prominent surface orientation emerging under typical growth conditions, has a slightly corrugated structure with two inequivalent Zn atomic sites exposed at the surface, see Figure 1. To make a distinction between the two sites, we call the Zn atoms on the ridges surface positions, Figure 1(a), and the Zn atoms in the valleys subsurface positions, Figure 1(b). We consider the TM substituted in different positions, the substituted positions labelled by the number are shown in Figure 2(a). The energy depicted is the relative energy of a TM atom substituting a Zn atom, as a function of position of the substituted atom, with substitution in a "bulk" position (in the middle of the slab) taken as zero. We observe that the TM substitutions are generally more stable at the surface than in the bulk, see Figure 2(b). The surface positions (labeled "0" in Figure 2) are 0.2-0.6 eV lower in energy than positions deeper down, whereas subsurface positions (labeled "1" in Figure 2) are 0.1-0.3 eV lower in energy for most TM substitutions. This would mean that dopant atoms preferentially reside at the surface, where they can be catalytically active. The exception is substitution by Mn, whose energy is practically independent of position. Positions of Zn atoms deeper down in the slab play no role, as they show no catalytic activity. To study catalytic activity, we substitute a surface or a subsurface Zn atom by a TM atom. In addition, we also consider simultaneous substitutions at both these positions.
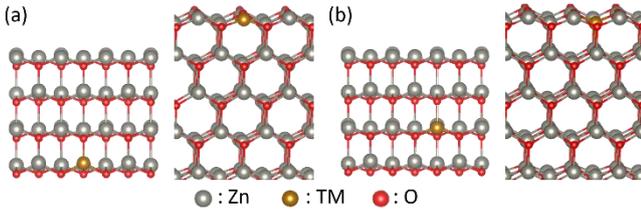
Figure 1. Top and side views of the atomic structures of (a) the TM doped ZnO surface and (b) the TM doped ZnO subsurface.
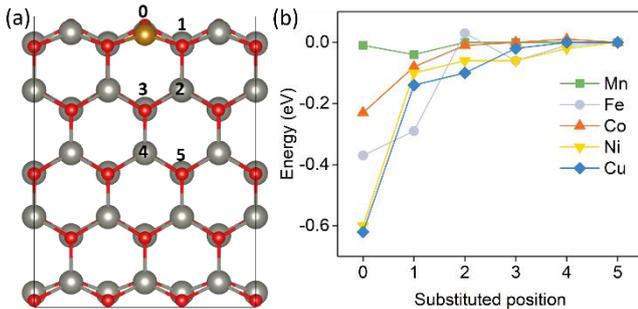
Figure 2. (a) Side view of the substituted positions of the TM in ZnO $(10\bar{1}0)$ surface, (b) total energy in different substituted positions, the x axis indicates the substituted position. We assume the total energy of TM substitutes in the bulk (i.e. substituted position 5) as 0, negative values mean that other substitutions show lower total energy than TM substitutes in the bulk, which are more stable than position 5 substitution.

Having established the relative stability of the TM dopant positions, their overall stability can be assessed through their formation free energies[28]

$$\Delta E_{\text{form}} = E_{\text{TM/ZnO}} - E_{\text{ZnO slab}} - \mu_{\text{TM}} + \mu_{\text{Zn}}, \quad (14)$$

where $E_{\text{TM/ZnO}}$ and $E_{\text{ZnO slab}}$ are the total energies of the ZnO slab doped with one TM atom, and that of the pure ZnO slab, respectively, and μ_{TM} and μ_{Zn} are the chemical potentials of the TM and of Zn, respectively. For μ_{TM} we use the total energy of the

bulk TM in its most stable structure. To calculate μ_{Zn}, we assume oxygen-rich conditions, where ZnO and oxygen gas are in equilibrium, as is appropriate for the OER

$$\mu_{\text{Zn}} = E_{\text{ZnO bulk}} - \frac{1}{2}\mu_{\text{O}_2(g)}. \quad (15)$$

Here $E_{\text{ZnO bulk}}$ is the total energy per formula unit of bulk ZnO, and $\mu_{\text{O}_2(g)}$ is the chemical potential of oxygen gas at standard conditions ($T = 298$ K and $P = 1$ bar), which is calculated as in Ref.[29] A negative formation energy ΔE_{form} indicates the TM doped system is stable.

The formation energies of TM doped ZnO, with the TM atoms in surface and subsurface positions are shown in Figure 3. It shows clearly that, although the stability of the doped systems decreases if one goes down the TM series from Mn to Cu, all systems are in fact stable.
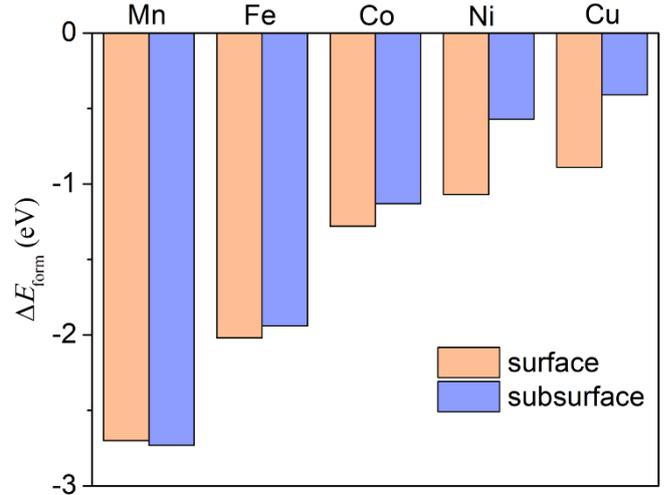
Figure 3. Formation free energies, Eqs (14) and (15), of TM dopant atoms in ZnO in surface and subsurface positions.

The OER intermediate species OH, O, and OOH, reactions (2)-(5) can adsorb on the ZnO $(10\bar{1}0)$ surface in a variety of bonding configurations. Bridge-site adsorption involves bonding of the species to the TM and an adjacent surface Zn atom, see Figures 4(a) and (b), whereas top-site adsorption involves bonding to the TM atom only, see Figure S5. The OH and O species can be adsorbed both on bridge and top sites, if the TM dopant atom is at a Zn surface position and both these bonding geometries are locally stable. However, the total energies of these OER intermediates adsorbed on bridges site are always lower than adsorbed on top sites. Therefore, we only discuss bridge-site adsorption in the following, whereas top-site adsorption is discussed in the Supporting Information.
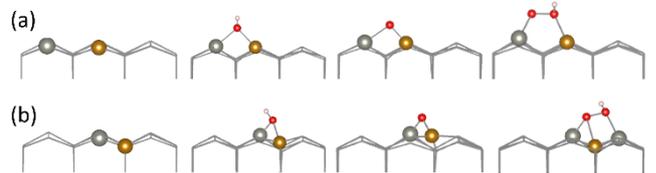
Figure 4. The atomic structures without and with OER intermediates are shown for (a) surface and (b) subsurface TM doping. The structures from left to right are in the sequence of vacant site (*), *OH, *O, and *OOH. Only the case for bridge site adsorption is shown.

We find that for a TM dopant atom at a Zn subsurface position, OH and O only adsorb in a bridge configuration, and on-top adsorption is not stable. For the adsorption of the OOH species, we have identified three different (meta)stable bridge-site configurations, both for TM dopants in the Zn surface and in the Zn subsurface positions, see Figure S6. In the following we will

only discuss the results pertaining to the most stable bonding configurations. Results for other, metastable, configurations can be found in the Supporting Information, see Tables S4 and S5.

The structures shown in Figure 4 have the Zn atoms at the surface exposed, whereas under alkaline conditions they may be covered by hydroxyl (OH) groups. Figure S7 in the Supporting Information shows a calculated Pourbaix diagram,[30] which demonstrates that under usual operating conditions (U and pH) hydroxylation is only partial, such that the OER is not hindered. Hydroxylation of the TM active site is required for the first step in the OER anyway, see Eq (2).
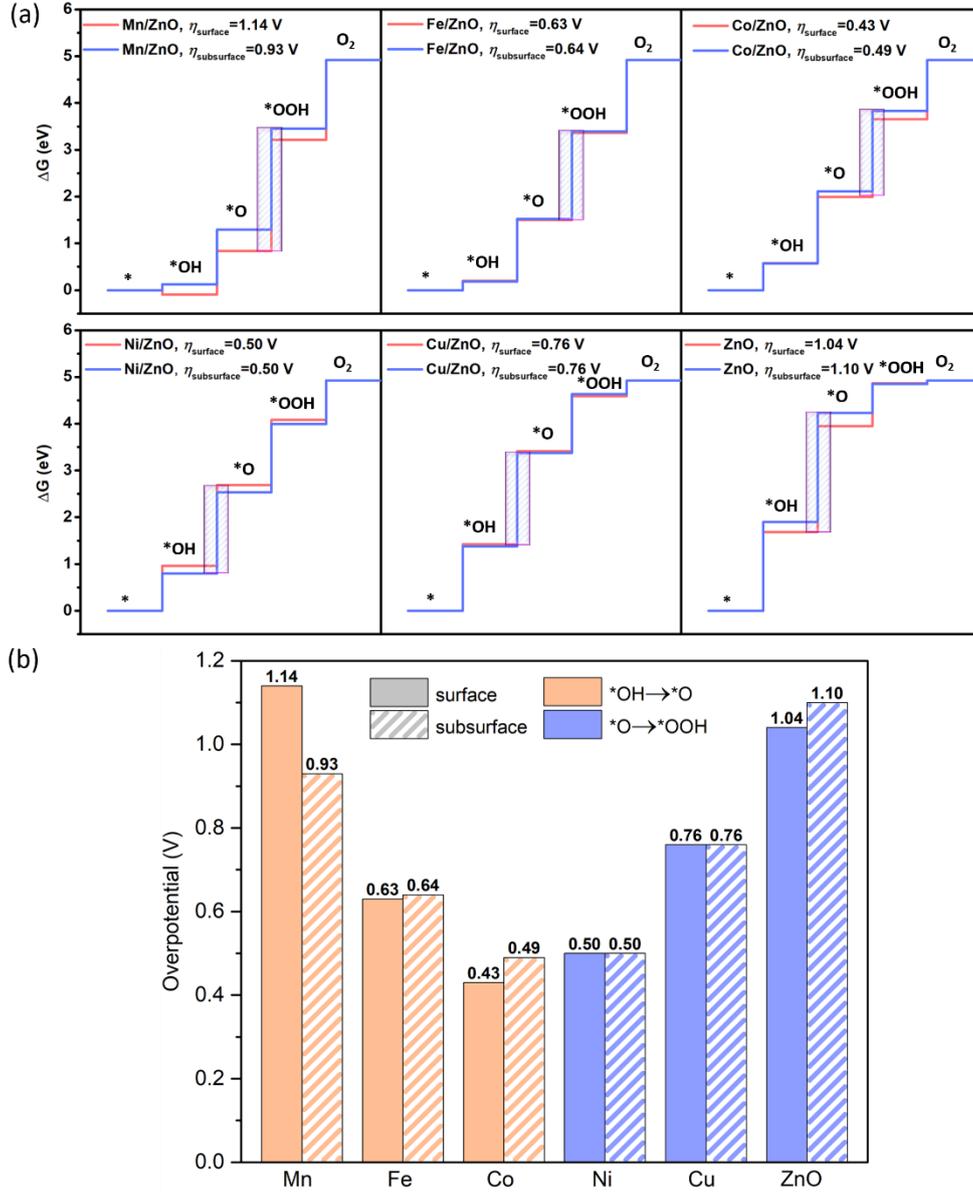
Figure 5. (a) Gibbs free energy diagrams of pristine and TM doped ZnO surface and subsurface systems. The purple-shaded fields indicate the potential determining steps. The overpotentials are given in the legends; $\eta_{surface}$ and $\eta_{subsurface}$ represent the overpotentials of surface and subsurface doped systems, respectively. (b) Summary plot of the overpotential for the different TM dopants on surface and subsurface. The potential determining steps are represented by different colors.

Gibbs Free Energies and Overpotentials

We calculate the Gibbs free energies, Eqs (7)-(10), of the four reaction steps (2)-(5) for the pristine and for the TM-doped ZnO $(10\bar{1}0)$ surface. The results are shown in Figure 5(a). According to the sum rule, Eq (11), the Gibbs free energy difference between the initial plateau, marked *, and the final plateau, marked O2, is fixed at 4.92 eV.[31] The corresponding calculated overpotentials, Eq (13), are summarized in Figure 5(b). The overpotentials range from 0.43 V to 1.14 V. The potential determining step for the first half of the series (Mn, Fe, Co) is the formation of *O, whereas for the second half of the series (Ni, Cu, Zn), it is the *OOH formation. As we move from left to right through the 3d series (Mn to Zn), the overpotential first decreases, reaches a minimum, and then increases again. The overpotentials for the surface and subsurface substitutional sites are generally similar, where only in the Mn case there is a significant difference.

5

Pristine ZnO shows large overpotentials of 1.04 V and 1.10 V for surface and subsurface sites, which is in agreement with the observed low activity of ZnO regarding the OER.[14] The lowest overpotentials, 0.43 V and 0.49 V, are obtained for surface and subsurface Co substitution. Ni substitution is a close second, with an overpotential of 0.50 V, whereas Fe substation gives an overpotential that is ~0.1 V higher than that of Ni. Cu substitution leads to a significant overpotential of 0.76 V, and Mn substitution gives virtually no improvement over pristine ZnO.

Park at al.[14] have studied composites of ZnO and TM oxides for the OER, where they have observed that mixing ZnO with Co oxide gives an overpotential ~0.4 V, whereas mixing with Ni and Fe oxides gives an overpotential that is ~0.2 V higher, and mixing with Mn oxide leads to an overpotential comparable to that of Fe and Ni. A direct comparison is difficult, however, as the TMs in their native oxides typically have an oxidation state and oxygen coordination that is different from our substitutional TM atoms, which likely alters their catalytic activity. Note that substitutional doping is aimed at maintaining the good conductive properties of the ZnO matrix, whereas those can be affected in a major way if one considers composite materials.

Binding Energies of Adsorbed Species

To interpret the trends in the calculated overpotentials, we focus on the free energies of the individual adsorbed intermediate species.[16a] The Gibbs free energies of the OER intermediates can be calculated from Eqs (7)-(10) for $U = 0$.

$$\Delta G_{*OH} = \Delta G_1 = E_{*OH} - E_* - E_{H_2O} + \frac{1}{2}E_{H_2} + (\Delta ZPE - T\Delta S)_1, \quad (16)$$

$$\Delta G_{*O} = \Delta G_1 + \Delta G_2 = E_{*O} - E_* - E_{H_2O} + E_{H_2} + (\Delta ZPE - T\Delta S)_{1+2}, \quad (17)$$

$$\Delta G_{*OOH} = \Delta G_1 + \Delta G_2 + \Delta G_3 = E_{*OOH} - E_* - 2E_{H_2O} + \frac{3}{2}E_{H_2} + (\Delta ZPE - T\Delta S)_{1+2+3}. \quad (18)$$

The free energies of the OER intermediates, ΔG_{*OH}, ΔG_{*O}, and ΔG_{*OOH}, are plotted in Figures 6(a) and (b) for TM surface and subsurface dopants. The lower the free energy, the stronger the bonding of the intermediate to the active site on the substrate. All ΔG_{*OH}, ΔG_{*O}, and ΔG_{*OOH} curves show a similar trend. We find that all free energies monotonically increase as we go down the 3d series from Mn to Zn, meaning that the bonding between intermediate and substrate becomes weaker, which is consistent with previous studies.[16a, 32]

The ideal values for ΔG_{*OH}, ΔG_{*O}, and ΔG_{*OOH} are $\Delta G_0/4 = 1.23$ eV, $\Delta G_0/2 = 2.46$ eV, and $3\Delta G_0/4 = 3.69$ eV, respectively, as then the overpotential $\eta = 0$ V, according to Eqs (12), (13), and (16)-(18). These ideal values are indicated by horizontal dashed lines in Figures 6(a) and (b). For the TM dopant series we find $\Delta G_{*OH} < \Delta G_0/4$ for Mn to Ni, and $\Delta G_{*OH} > \Delta G_0/4$ for Cu and Zn, where Ni and Cu are closest to the ideal value for ΔG_{*OH}. The elements before Ni (i.e., Mn to Co) give too strong a bonding to OH, whereas the element after Cu (i.e., Zn) gives too weak a bonding.

ΔG_{*O} shows a similar monotonic behavior as ΔG_{*OH}, but it has a stronger dependence on the TM dopant atom. Comparison to the ideal value $\Delta G_0/2 = 2.46$ eV (the horizontal yellow dashed lines in Figures 6(a) and (b)) shows that Mn and Fe bind the O atom too strongly, with $\Delta G_{*O} < 2.0$ eV, and Cu and Zn bind O too weakly, with $\Delta G_{*O} > 3.0$ eV. From the perspective of ΔG_{*O}, Co and Ni dopants are the most suitable for the OER. The ΔG_{*OOH} curves are similar in shape to the ΔG_{*OH} curves, with a similar decrease in bonding strength of the adsorbed species for the TM dopant

series from Mn to Zn. The ΔG_{*OOH} for Co is very close to the ideal value $3\Delta G_0/4 = 3.69$ eV (the horizontal green dashed lines in Figures 6(a) and (b)), making the Co dopant most optimal for the OER regarding the bonding to OOH.

From these results one concludes that there is not a single TM dopant that gives an optimal bonding to all intermediate species, OH, O, and OOH, such that it leads to a zero overpotential. Overall the best TM dopants are Co, which binds OH and O slightly too strongly, but is perfect for OOH, and Ni, which is almost perfect for OH, but binds O and OOH lightly too weakly. The elements before Co (i.e., Mn, Fe) tend to bind the intermediate species too strongly, and the elements after Ni (i.e., Cu, Zn) give too weak a bonding.
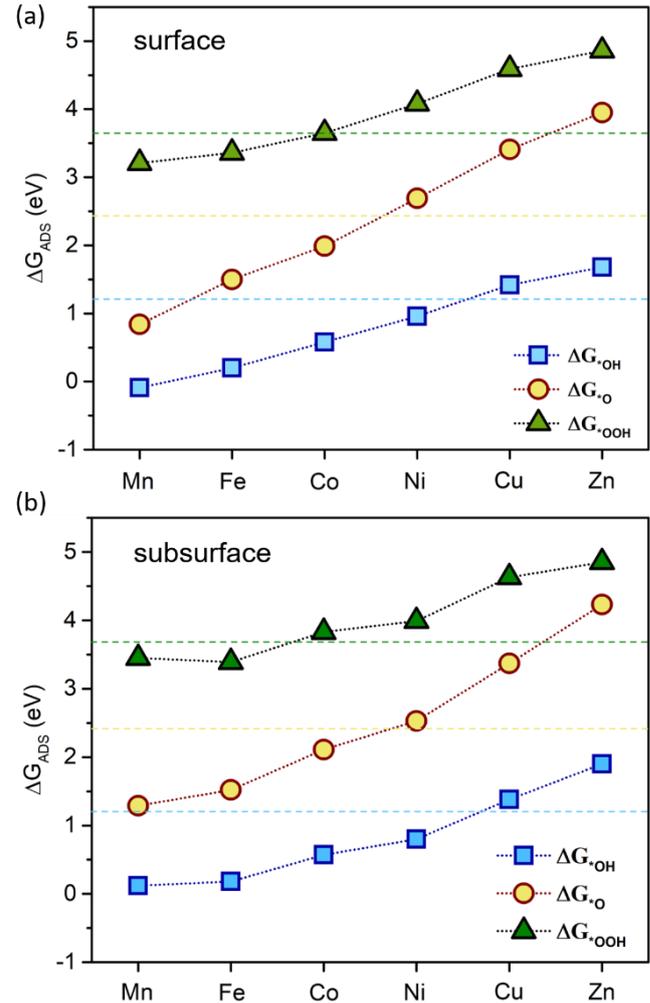
Figure 6. Gibbs free energies of the OER intermediates on TM doped and pristine ZnO $(10\bar{1}0)$ (a) surface and (b) subsurface. Adsorbed species are abbreviated as ADS and signifies *OH (blue squares), *O (yellow circles), and *OOH (green triangles). The blue, yellow, and green dashed horizontal lines stand for the Gibbs free energies 1.23, 2.46, and 3.69 eV, respectively.

Analysis of Overpotential

In Figure 5, we observe that for all TM dopants the overpotential is determined by one of the two middle steps, ΔG_2 or ΔG_3, i.e., the formation of *O from *OH, or the formation of *OOH from *O. In Figure 6, we notice that the ΔG_{*OH} and ΔG_{*OOH} curves run almost parallel. One can connect the two observations by focusing upon the Gibbs free energy difference between the bonding of the OH and the OOH species

$$\Delta G_{23} = \Delta G_{*OOH} - \Delta G_{*OH} = \Delta G_2 + \Delta G_3, \quad (19)$$

according to Eqs (16) and (18). To obtain a zero overpotential, ideally $\Delta G_{23} = \Delta G_0/2 = 2.46$ eV, according to Eq (12). It has been observed that for most TM oxides $\Delta G_{23} \approx 3.2$ eV, irrespective of the TM.[31-33] In many of these cases, both the OH and OOH species are bonded to the active catalytic site by a single bond to the (terminal) O atom, and the relatively materials independent ΔG_{23} is thought to reflect the notion that the two bonds from OH or OOH to any TM are very similar to one another.

It is useful to see whether the cases we study here fall within the same scheme. At first sight, the bonding of the OH and OOH species to the substrate are quite different. The O atom of OH forms bridge bonds to the TM dopant and a Zn atom of the substrate, whereas for OOH, one of the O atoms binds to the TM dopant, and the other O atom binds to a substrate Zn atom, see Figures 4(a) and (b). Nevertheless, the calculated ΔG_{23} are remarkably similar for the different TM dopants, as shown in Figure 7. Moreover, they are all significantly larger than the ideal value of 2.46 eV. In fact, the average ΔG_{23} for surface/subsurface TM dopants is 3.17/3.20 eV, with a standard deviation of 0.07/0.12 eV, which is strikingly similar to the results obtained for pure TM oxides, such as Co_3O_4 and NiO.[31]

(a)

(b)
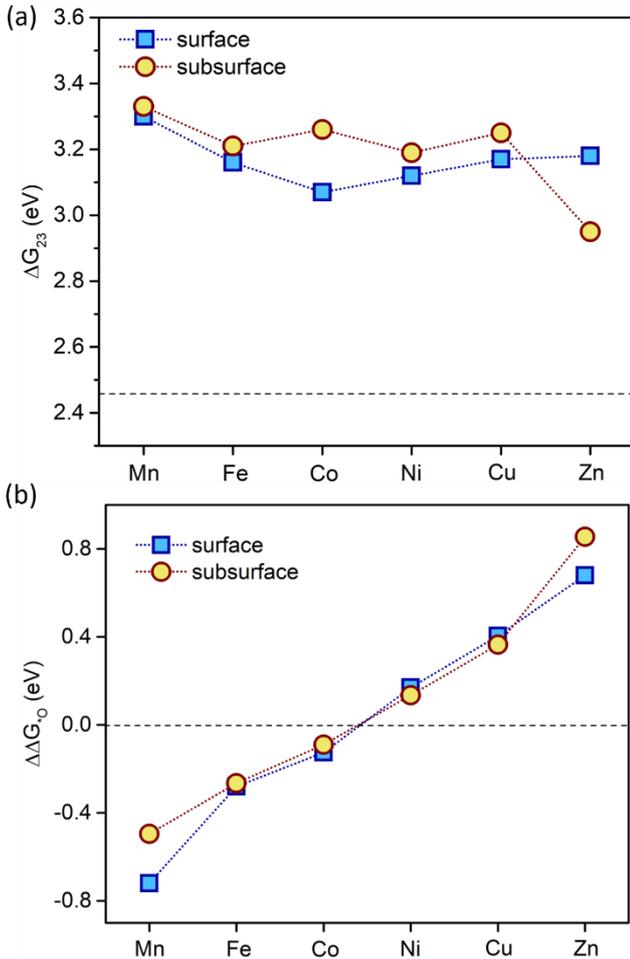
Figure 7. (a) The Gibbs free energy difference ΔG_{23} on TM doped and pristine ZnO $(10\bar{1}0)$ surface and subsurface; the dashed horizontal line indicates the ideal value of $2G_0 = 2.46$ eV. (b) The Gibbs free energy difference $\Delta\Delta G_{*O}$ on TM doped and pristine ZnO $(10\bar{1}0)$ surface and subsurface; the value larger than 0 eV indicates weak O adsorption and smaller than 0 eV indicates strong O adsorption; the dashed horizontal line indicates the optimal value of 0 eV. The lines between data points are added to guide the eye.

Any excess of ΔG_{23} over 2.46 eV contributes to the overpotential. According to Eq (12), the minimum overpotential resulting from Eq (19) is

$$\eta_{23} = (\Delta G_{23} - \Delta G_0/2)/(2e). \tag{20}$$

Based on the data shown in Figure 7(a), η_{23} ranges between 0.30 V and 0.42 V for surface doping and between 0.25 V and 0.44 V for subsurface doping, which are all values that are relatively close to one another. For a TM surface dopant, the minimum η_{23} is for Co and for a TM subsurface dopant it is for Zn.

The quantity η_{23} gives a lower bound to the overpotential in case $\Delta G_2 = \Delta G_3$. In case $\Delta G_2 \neq \Delta G_3$, and assuming that one of these steps determines the overpotential η, Eq (13), one can rewrite the latter as

$$\eta = \eta_{23} + |\Delta\Delta G_{*O}|/e, \tag{21}$$

where $\Delta\Delta G_{*O}$ measures the binding energy of the O species relative to the average binding energy of the OH and OOH species

$$\Delta\Delta G_{*O} = \Delta G_{*O} - \tfrac{1}{2}(\Delta G_{*OH} + \Delta G_{*OOH}) = \tfrac{1}{2}(\Delta G_2 - \Delta G_3). \tag{22}$$

According to Eq (21), $\Delta\Delta G_{*O}$ should ideally be zero, and the more it deviates from zero, the larger the overpotential. Figure 7(b) shows $\Delta\Delta G_{*O}$, calculated for the TM dopant series. It shows a monotonic behavior along the series, starting with $\Delta\Delta G_{*O} < 0$ for Mn and increasing to $\Delta\Delta G_{*O} > 0$. The most interesting TM dopants are Co and Ni, as there $\Delta\Delta G_{*O}$ is closest to zero. For these dopants, the binding energy of O is closest to the average of the binding energies of OH and OOH. For Mn and Fe dopants, the O binding is too strong, resulting in $\Delta\Delta G_{*O} < 0$, and for the Cu dopant and pristine ZnO, the O binding is too weak, which gives $\Delta\Delta G_{*O} > 0$. The optimal TM dopants are then Co and Ni, where the overpotential $\eta \approx \eta_{23}$.

Double Transition Metal Substitutions

If the doping concentration is increased, one will encounter more frequently a situation where two adjacent Zn atoms at the surface are replaced by TM atoms, see Figure 8. We will call this "double doping" in the following. As the adsorbed intermediate species of the OER generally form bridge bonds to the metal atoms of the substrate, they can simultaneously bind to two TM dopants, instead of to one TM dopant and one Zn atom, compare to Figure 4. It is instructive to investigate whether this altered bonding scheme can change the overpotential. Again, there are two possible configurations of interest, one where two adjacent Zn atoms at the surface ridges are replaced by TM atoms, and another where one such Zn atom and one adjacent valley Zn atom are replaced. We call these the "surface" and "subsurface" configurations, respectively, see Figure 8.

The total energies of the ZnO slab doped with two TM atoms in adjacent surface positions, one in a surface position and one in an adjacent subsurface position are listed in Tables S8 and S9, respectively. The relative stability of double TM doped systems with respect to single TM doped systems is investigated by focusing on the binding energy. The net interaction between the dopants is in most cases $\lesssim 0.1$ eV, see Figure S8 of the Supporting Information, which means that the driving force for clustering is small.
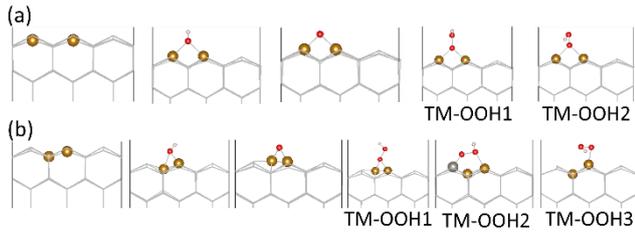
Figure 8. Side views of the double TM doped ZnO (a) surface doping; the sequence is nothing adsorbed, OH, O, and OOH adsorbed; after relaxation, the OOH shows two configurations, TM-OOH1 and TM-OOH2; (b) subsurface doping; the sequence is nothing adsorbed, OH, O and OOH adsorbed. After relaxation, the OOH shows three configurations, TM-OOH1, TM-OOH2, and TM-OOH3.

As before, the OER intermediate species can bind in several configurations, where a number of possibilities are shown in Figure 8. A full list of the calculated total energies of those configurations is given in Table S10 and Table S11 of the Supporting Information. In the following we only use the configurations with the lowest total energy.

A summary of the calculated overpotentials resulting from the double TM substitution is given in Figure 9, whereas the Gibbs free energies of all intermediate steps, ΔG_{1-4}, are shown in in Figure S9. Comparison to single TM substitution (refer to Figure 5(b)) shows that the overpotentials of single and double substitution are of a similar magnitude. However, the minimum overpotential is shifted from Co/Ni in the single substitution case to Ni/Cu in the double substitution, where in both cases the minimum occurs around the point where the third step of the OER, Eq (9), takes over as the overpotential determining step from the second step of the OER, Eq (8). As the O intermediate species is common in both of these steps, this is an indication that the bonding of the O atom to the substrate is mainly responsible for the difference in overpotentials between single (Figure 5(b)) and double (Figure. 9) substitution.
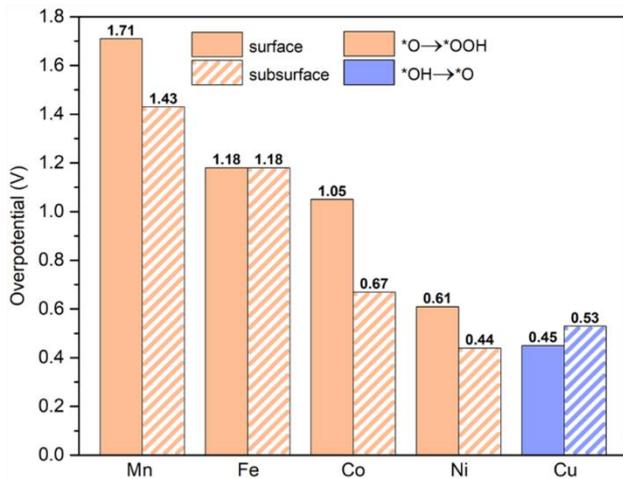
Figure 9. Summary plot of the overpotential for the different TM dopants in the case of double TM doping on surface and subsurface. The potential determining steps are represented by different colors.

The individual Gibbs free adsorption energies of the OER intermediates on double TMs doped ZnO ($10\bar{1}0$) surface and subsurface can be found in the Supporting Information, Figure S10. We can analyze the overpotential η resulting from the double substitution in terms of ΔG_{23} and $\Delta\Delta G_{*O}$, as in the previous section, Eq (21). ΔG_{23} reflects the difference in the bonding of the OH and the OOH species to the substrate, Eq (19). Plotted in Figure 10(a), it displays a little more variation with the TM dopant than for the single substitution case, compare to Figure 7(a). Nevertheless, also for double TM substitution, the values of ΔG_{23} are still significantly larger that the ideal value $\Delta G_0/2 = 2.46$ eV, which results in a contribution to the overpotential, Eq (20).

The second contribution $\Delta\Delta G_{*O}$ to the overpotential, Eqs (21) and (22), reflecting the adsorption strength of the O species with respect to the average of the OH and OOH species, is plotted in Figure 10(b). $\Delta\Delta G_{*O}$ increases monotonically going down the TM series from Mn to Cu, which is similar to the single TM dopant case, shown in Figure 7(b). However, for the double TM dopant case, Figure 10(b), the $\Delta\Delta G_{*O}$ values are significantly smaller, indicating a bonding of the O species to the two TM dopant atoms that is much stronger than the bonding to a single TM dopant (and a Zn atom of the substrate).

To obtain a low overpotential one needs $\Delta\Delta G_{*O} \approx 0$, Eq (21), which only occurs for the late TM dopants Ni and Cu. So, qualitatively the difference between the overpotentials for the single TM dopant, Figure 5(b), and the double TM dopant, Figure 9, is due to the stronger bonding of the O intermediate species to the substrate.

Alternative ways to analyze the overpotential for metal electrodes make use of scaling relations to, for instance, the electrochemical-step symmetry index (ESSI).[34] In the present case the results regarding the use of the ESSI as a descriptor does not give further insight, see Supporting Information, Figure S11.
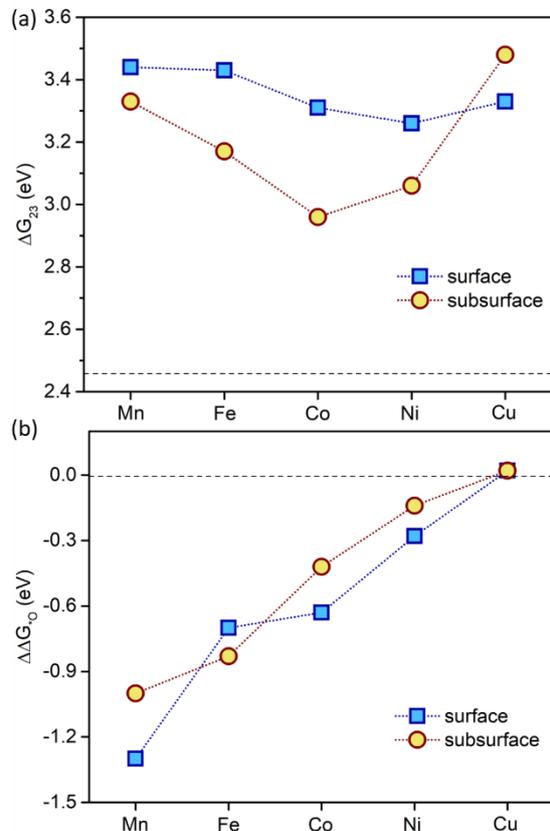
Figure 10. (a) The Gibbs free energy difference ΔG_{23} on double TMs doped ZnO ($10\bar{1}0$) surface and subsurface; the dashed horizontal line indicates the ideal value of $2G_0 = 2.46$ eV. (b) The Gibbs free energy difference $\Delta\Delta G_{*O}$ on double TMs doped ZnO ($10\bar{1}0$) surface and subsurface; the value larger than 0 eV

indicates weak O adsorption and smaller than 0 eV indicates strong O adsorption; the dashed horizontal line indicates the optimal value of 0 eV. The lines between data points are added to guide the eye.

Summary and Concluding Discussion

We computationally investigate the electrochemical activity under alkaline conditions of the ZnO ($10\bar{1}0$) surface substitutionally doped with transition metals (TMs) of the 3d series. Varying the TM and the doping site, we find that Co doping gives the minimum calculated overpotential, which is between 0.43 V and 0.49 V. In addition, Ni doping also gives a low overpotential of 0.50 V, whereas Fe or Cu doping give smaller improvements over pure ZnO regarding the OER activity. Mn gives practically no improvement at all.

TMs dopants from the second half of the 3d series are more often found to improve the OER performance of oxides and nitrides. For instance, Liao et al.[3b] have calculated that Co and Ni dopants lower overpotential of pure hematite (Fe_2O_3), and Zaffran and Toroker[35] have concluded that Fe, Co, or Cu doping significantly lowers the overpotential of NiOOH. In our previous work on two-dimensional AlN and GaN,[16a] we found that in particular Ni doping lowers the overpotential.

Liao et al.[3b] correlated the lowering of the overpotential of hematite upon Co and Ni doping with Co or Ni dopants being less positively charged than the host Fe atoms, resulting in a more optimal bonding to the OER intermediates. We have calculated the Bader charges of pristine and TM doped ZnO surfaces, see Sec 2.6, Table S7 in the Supporting Information, but observed no distinct correlation between the overpotential and these Bader charges. In our work on TM doped 2D AlN/GaN, we observed that the low overpotential found for Ni doping correlates with a transition from a high-spin to a low-spin state on the Ni atom.[16a] In TM doped ZnO, it turns out that all TM dopants remain in high-spin states, with or without adsorbed OER intermediate species.

For TM oxides, it has been observed that the difference in adsorption free energy of the OH and OOH is fairly constant for most TM species, $\Delta G_{23} = \Delta G_{*OOH} - \Delta G_{*OH} = 3.2 \pm 0.2$ eV.[31-33] We find that this result is also valid for TM doped ZnO, irrespective of the TM or of the details of the TM-OH or TM-OOH bonding configurations. This results in a minimum overpotential in the range $\eta_{23} = 0.27\text{-}0.47$ V, Eqs (20) and (21), for all TM dopants. The second factor contributing to the overpotential is the adsorption free energy of the O species, $\Delta\Delta G_{*O}$, relative to that of the OH and OOH species, Eq (22), which ideally should be zero. Going down the 3d TM series, $\Delta\Delta G_{*O}$ increases monotonically. For TM doped ZnO, $\Delta\Delta G_{*O}$ crosses zero between Co and Ni for single surface or subsurface TM dopant atoms. This is the parameter that can be varied most by changing the TM or the bonding configuration of the adsorbents.

Computational Methods

We use the Vienna ab initio package (VASP) to carry out DFT calculations within the projector-augmented wave (PAW) approach.[36] The exchange-correlation function is treated within the generalized gradient approximation (GGA) with the form developed by Perdew, Burke, and Ernzerhof (PBE).[37] We use a plane wave basis with an energy cutoff of 500 eV.

We start from the wurtzite structure of ZnO, and model the (non-polar) ($10\bar{1}0$) surface, which is the surface orientation that emerges under most growth conditions, as it is more stable than other (non-polar and polar) surfaces.[38] The ($10\bar{1}0$) surface is modeled by a (periodic) five-layer slab, using an in-plane 3×2 supercell, comprising 120 atoms, with a vacuum spacing of 15 Å between the periodic images of the slab to avoid spurious interactions. To model doping, one or two of the zinc atoms are replaced by TM atoms. The structure we use is shown in Figure 1. We use the top surface of the slab to model the OER, where the top three layers of the (doped) ZnO substrate, as well as the adsorbates, are fully relaxed until the maximum force on each atom is less than 0.01 eV/Å, while keeping the bottom two layers fixed. We use a dipole correction[39] and set the energy convergence criterion to 1×10^{-5} eV. The surface Brillouin zone is sampled using a $2 \times 2 \times 1$ Monkhorst-Pack k-point mesh for all calculations.[40]

In calculating Gibbs free energies of the adsorbed species, we incorporate zero-point energy (ZPE) and entropy corrections. The $\text{ZPE} = \sum_i \frac{1}{2} h v_i$, where h is Planck's constant, are obtained from the calculated frequencies (v_i) of all vibrations of the atoms in the slab. The vibrational contribution to the entropy S of the molecules and the adsorbed species can be calculated in the usual way from these frequencies,[41] using temperature T = 298 K.[42] We used gas-phase H_2O at 0.035 bar and this temperature as the reference state for water molecules, which is in equilibrium with liquid water at standard temperature (T = 298 K). The entropy of H_2O gas is then taken from ref.[42], as are the entropies under standard conditions of the other gas-phase molecules. In the solid state, volume changes are typically very small, and therefore the small difference between enthalpy and energy is not considered.[16a] We have refrained from modeling solvation effects.

Acknowledgements

[1]   a) E. Fabbri, A. Habereder, K. Waltar, R. Kötz, T. J. Schmidt, *Catal. Sci. Technol.* **2014**, *4*, 3800-3821; b) J. Joo, T. Kim, J. Lee, S. I. Choi, K. J. A. M. Lee, *Adv. Mater.* **2019**, *31*, 1806682; cC. Hu, L. Zhang, J. J. E. Gong, E. Science, *Energy Eniviron. Sci.* **2019**, *12*, 2620-2645.

[2]   X. Zhang, A. Bieberle‐Hütter, *ChemSusChem* **2016**, *9*, 1223-1242.

[3]   a) M. C. Toroker, *J. Phys. Chem. C* **2014**, *118*, 23162-23167; b) P. Liao, J. A. Keith, E. A. Carter, *J. Am. Chem. Soc.* **2012**, *134*, 13296-13309.

[4]   a) Y. Lee, J. Suntivich, K. J. May, E. E. Perry, Y. Shao-Horn, *J. Phys. Chem. Lett.* **2012**, *3*, 399-404; b) H. G. Sanchez Casalongue, M. L. Ng, S. Kaya, D. Friebel, H. Ogasawara, A. Nilsson, *Angew. Chem. Int. Edit.* **2014**, *53*, 7169-7172; *Angew. Chem. 2014*, *126*, 7297-7300; c) R. R. Rao, M. J. Kolb, N. B. Halck, A. F. Pedersen, A. Mehta, H. You, K. A. Stoerzinger, Z. Feng, H. A. Hansen, H. J. E. Zhou, E. Science, *Energy Eniviron. Sci.* **2017**, *10*, 2626-2637.

[5]   a) Y. Zhang, B. Ouyang, J. Xu, G. Jia, S. Chen, R. S. Rawat, H. J. Fan, *Angew. Chem. Int. Edit.* **2016**, *55*, 8670-8674; *Angew. Chem. 2016*, *128*, 8812-8816; b) P. Chen, K. Xu, Z. Fang, Y. Tong, J. Wu, X. Lu, X. Peng, H. Ding, C. Wu, Y. Xie,

Angew. Chem. Int. Edit. **2015**, *54*, 14710-14714; *Angew. Chem. 2016*, **127**, 14923-14927.

[6] a) K. Liu, C. Zhang, Y. Sun, G. Zhang, X. Shen, F. Zou, H. Zhang, Z. Wu, E. C. Wegener, C. J. Taubert, *ACS Nano* **2018**, *12*, 158-167; b) J. Xu, J. Li, D. Xiong, B. Zhang, Y. Liu, K.-H. Wu, I. Amorim, W. Li, L. Liu, *Chemical science* **2018**, *9*, 3470-3476; c) M. Meng-JungáLi, L. Y. SukáLee, S. C. EdmanáTsang, *Chem. Commun.* **2018**, *54*, 8630-8633.

[7] Y. Zhao, G. Brocks, H. Genuit, R. Lavrijsen, M. A. Verheijen, A. Bieberle‐Hütter, *Adv. Energy Mater.* **2019**, *9*, 1900940.

[8] a) L. Zeng, K. Sun, X. Wang, Y. Liu, Y. Pan, Z. Liu, D. Cao, Y. Song, S. Liu, C. Liu, *Nano Energy* **2018**, *51*, 26-36; b) Y. Zhu, H. Yang, K. Lan, K. Iqbal, Y. Liu, P. Ma, Z. Zhao, S. Luo, Y. Luo, J. Ma, *Nanoscale* **2019**, *11*, 2355-2365; c) G. Zhang, Y.-S. Feng, W.-T. Lu, D. He, C.-Y. Wang, Y.-K. Li, X.-Y. Wang, F.-F. Cao, *ACS Catal.* **2018**, *8*, 5431-5441.

[9] a) Á. Morales-García, F. Calle-Vallejo, F. Illas, *ACS Catal.* **2020**, *10*, 13487-13503; b) B. Anasori, M. R. Lukatskaya, Y. Gogotsi, *Nat. Rev. Mater.* **2017**, *2*, 16098; c) H. Oschinski, Á. Morales-García, F. Illas, *J. Phys. Chem. C* **2021**, *125*, 2477-2484.

[10] a) H. Osgood, S. V. Devaguptapu, H. Xu, J. Cho, G. Wu, *Nano Today* **2016**, *11*, 601-625; b) Y. Dou, T. Liao, Z. Ma, D. Tian, Q. Liu, F. Xiao, Z. Sun, J. H. Kim, S. X. Dou, *Nano Energy* **2016**, *30*, 267-275.

[11] A. Janotti, C. G. Van de Walle, *Rep. Prog. Phys.* **2009**, *72*, 126501.

[12] A. Kołodziejczak-Radzimska, T. J. M. Jesionowski, *Materials* **2014**, *7*, 2833-2881.

[13] C. B. Ong, L. Y. Ng, A. W. Mohammad, *Renew. Sust. Energy Rev.* **2018**, *81*, 536-551.

[14] D. M. Jang, I. H. Kwak, E. L. Kwon, C. S. Jung, H. S. Im, K. Park, J. Park, *J. Phys. Chem. C* **2015**, *119*, 1921-1927.

[15] a) K. Qi, X. Xing, A. Zada, M. Li, Q. Wang, S.-y. Liu, H. Lin, G. Wang, *Ceram. Int.* **2020**, *46*, 1494-1502; b) G. Wang, L. Zhang, Y. Li, W. Zhao, A. Kuang, Y. Li, L. Xia, Y. Li, S. Xiao, *J. Phys. D. Appl. Phys.* **2019**, *53*, 015104.

[16] a) Q. Liang, G. Brocks, X. Zhang, A. Bieberle-Hütter, *J. Phys. Chem. C* **2019**, *123*, 26289-26298; b) Q. Wang, X. Huang, Z. L. Zhao, M. Wang, B. Xiang, J. Li, Z. Feng, H. Xu, M. Gu, *J. Am. Chem. Soc.* **2020**, *142*, 7425-7433.

[17] C. Wang, G. Zhou, J. Li, B. Yan, W. Duan, *Phys. Rev. B* **2008**, *77*, 245303.

[18] a) A. Walsh, J. L. Da Silva, S.-H. Wei, *Phys. Rev. Lett.* **2008**, *100*, 256401; b) K. Harun, N. A. Salleh, B. Deghfel, M. K. Yaakob, A. A. Mohamad, *Results Phys.* **2020**, *16*, 102829; c) X. Ma, Y. Wu, Y. Lv, Y. Zhu, *J. Phys. Chem. C* **2013**, *117*, 26029-26039.

[19] C. Freysoldt, B. Grabowski, T. Hickel, J. Neugebauer, G. Kresse, A. Janotti, C. G. Van de Walle, *Rev. Mod. Phys.* **2014**, *86*, 253-305.

[20] S. Dudarev, G. Botton, S. Savrasov, C. Humphreys, A. Sutton, *Phys. Rev. B* **1998**, *57*, 1505.

[21] Ü. Özgür, Y. I. Alivov, C. Liu, A. Teke, M. Reshchikov, S. Doğan, V. Avrutin, S.-J. Cho, H, Morkoç, *J. Appl. Phys.* **2005**, *98*, 11.

[22] a) L. Wang, Z. Zeng, W. Gao, T. Maxson, D. Raciti, M. Giroux, X. Pan, C. Wang, J. J. S. Greeley, *Science* **2019**, *363*, 870-874; b) H. Wang, S. Xu, C. Tsai, Y. Li, C. Liu, J. Zhao, Y. Liu, H. Yuan, F. Abild-Pedersen, F. B. J. S. Prinz, *Science* **2016**, *354*, 1031-1036.

[23] F. Viñes, F. Illas, *J. Comput. Chem.* **2017**, *38*, 523-529.

[24] a) S. Zhou, N. Liu, Z. Wang, J. Zhao, *ACS Appl. Mater. Interfaces* **2017**, *9*, 22578-22587; b) X. Rong, J. Parolin, A. M. Kolpak, *ACS Catal.* **2016**, *6*, 1153-1158.

[25] a) J. Pfrommer, M. Lublow, A. Azarpira, C. Göbel, M. Lücke, A. Steigert, M. Pogrzeba, P. W. Menezes, A. Fischer, T. Schedel‐Niedrig, *Angew. Chem. Int. Edit.* **2014**, *53*, 5183-5187; *Angew. Chem. 2014,* **126**, 5283-5287; b) L. Zhuang, Y. Jia, T. He, A. Du, X. Yan, L. Ge, Z. Zhu, X. Yao, *Nano Res.* **2018**, *11*, 3509-3518.

[26] A. Bagger, I. E. Castelli, M. H. Hansen, J. Rossmeisl, in *Handbook of Materials Modeling: Applications: Current and Emerging Materials*, Springer, **2018**, pp. 1-31.

[27] Q. Liang, G. Brocks, A. Bieberle-Hütter, *J. Phys. Energy* **2021**, *3*, 026001.

[28] X. Luo, G. Wang, Y. Huang, B. Wang, H. Yuan, H. Chen, *J. Phys. Chem. C* **2017**, *121*, 18534-18543.

[29] M. García-Mota, A. Vojvodic, H. Metiu, I. C. Man, H.-Y. Su, J. Rossmeisl, J. K. Nørskov, *ChemCatChem* **2011**, *3*, 1607-1611.

[30] a) F. Calle-Vallejo, M. T. M. Koper, *Electrochim. Acta* **2012**, *84*, 3-11; b) H.-Y. Su, Y. Gorlin, I. C. Man, F. Calle-Vallejo, J. K. Nørskov, T. F. Jaramillo, J. Rossmeisl, *Phys. Chem. Chem. Phys.* **2012**, *14*, 14010-14022.

[31] I. C. Man, H. Y. Su, F. Calle‐Vallejo, H. A. Hansen, J. I. Martinez, N. G. Inoglu, J. Kitchin, T. F. Jaramillo, J. K. Nørskov, J. Rossmeisl, *ChemCatChem* **2011**, *3*, 1159-1165.

[32] F. Calle-Vallejo, J. I. Martínez, J. Rossmeisl, *Phys. Chem. Chem. Phys.* **2011**, *13*, 15639-15643.

[33] J. Rossmeisl, Z.-W. Qu, H. Zhu, G.-J. Kroes, J. K. Nørskov, *J. Electroanal. Chem.* **2007**, *607*, 83-89.

[34] O. Piqué, F. Illas, F. Calle-Vallejo, *Phys. Chem. Chem. Phys.* **2020**, *22*, 6797-6803.

[35] J. Zaffran, M. C. Toroker, *ChemistrySelect* **2016**, *1*, 911-916.

[36] a) P. E. Blöchl, *Phys. Rev. B* **1994**, *50*, 17953; b) G. Kresse, D. Joubert, *Phys. Rev. B* **1999**, *59*, 1758; c) G. Kresse, J. Furthmüller, *Phys. Rev. B* **1996**, *54*, 11169.

[37] J. P. Perdew, K. Burke, M. Ernzerhof, *Phys. Rev. Lett.* **1996**, *77*, 3865.

[38] X. Tian, J. Xu, W. Xie, *J. Phys. Chem. C* **2010**, *114*, 3973-3980.

[39] J. Neugebauer, M. Scheffler, *Phys. Rev. B* **1992**, *46*, 16067.

[40] H. J. Monkhorst, J. D. Pack, *Phys. Rev. B* **1976**, *13*, 5188.

[41] M. J. van Setten, G. A. de Wijs, G. Brocks, *Phys. Rev. B* **2008**, *77*, 165115.

[42] J. K. Nørskov, J. Rossmeisl, A. Logadottir, L. Lindqvist, J. R. Kitchin, T. Bligaard, H. Jonsson, *J. Phys. Chem. B* **2004**, *108*, 17886-17892.

Entry for the Table of Contents
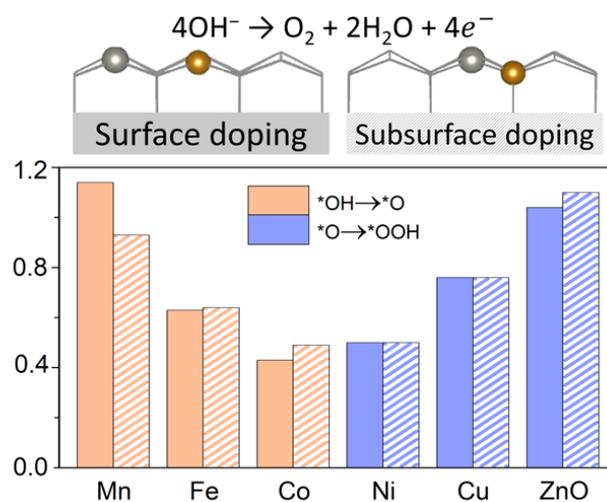
Transition metal doped surface and subsurface ZnO for oxygen evolution reaction under alkaline conditions. Co and Ni are promising dopants for increasing the oxygen evolution reaction activity of ZnO.